RSC Advances

PAPER

View Article Online
View Journal | View Issue

Cite this: *RSC Adv.*, 2025, **15**, 13728

Novel EDTA-chitosan/alginate porous composite beads for the removal of Pb(II) and methylene blue from aqueous solutions†

Xueling Liu, Wenjie Ren, Weilin Song, Wanqiang Zhang, Yuhan Wang, Yi Wang, Guozhi Fan, Lei Zhang* and Yanjun Huang*

Received 8th February 2025
Accepted 13th April 2025

DOI: 10.1039/d5ra00940e

rsc.li/rsc-advances

Wastewater containing heavy metals and organic dye pollutants discharged into receiving waters poses a serious environmental concern. Herein, a novel EDTA-chitosan/alginate porous composite bead adsorbent (EC–AB) was reported for the simultaneous removal of lead (Pb(II)) and methyl blue (MB) complexes from wastewater. Characterization results showed that EC–AB contained plenty of oxygen/nitrogen functional groups. The effect of $CaCO_3$ addition, pH of the initial solution, contact time, initial pollutant concentration, and ionic strength on EC–AB pollutant removal performance and the adsorption mechanism were systematically analyzed. These findings indicated that EC–AB exhibited high removal efficiency over a wide pH range and at high ionic strength. The maximum adsorption capacities of EC–AB for Pb(II) and MB were 504.11 mg g^{-1} and 660.76 mg g^{-1}, respectively, at 298 K. Adsorption kinetics and isotherm studies indicated that the adsorption well fitted the pseudo-second-order kinetic model and the Langmuir isotherm. A possible adsorption mechanism involving electrostatic attraction, chelation, ion exchange, H-bonding and synergistic effects was proposed. Moreover, EC–AB showed superior stability and reusability, with removal efficiencies of 76.64% for Pb(II) and 80.29% for MB after five continuous adsorption–desorption cycles for treating complex wastewater. In summary, this work provides a beneficial strategy for designing high-performance adsorbents for the treatment of wastewater.

1. Introduction

Wastewater containing metal ions and dyes released from the paint, paper, textile and electroplating industries poses a serious risk to the environment and human health.[1] The presence of heavy metal ions and dyes in wastewater is particularly concerning owing to their non-biodegradable nature and ability to bioaccumulate in the environment.[2] For instance, the heavy metal ion Pb(II) can cause kidney damage, neurological effects, dizziness, headaches, and irritability,[3–5] while excessive exposure to methylene blue (MB) may lead to various health issues such as abdominal pain, nausea, organ failure, dizziness, headaches, and excessive sweating.[6] Various processes can be employed to eliminate heavy metal ions and dyes from wastewater, such as chemical precipitation,[7] ion exchange,[8] membrane methods,[9,10] and electrochemical processes.[11,12] However, these technologies have limitations, such as low efficiency, high cost and high sludge volume.[13–16] Adsorption techniques are another option and offer the benefits of simple operation, low energy consumption, environmental friendliness, high process efficiency, and sustainable use of various natural materials, which make them suitable for a wide range of wastewater treatment applications.[17,18]

Chitosan (CS), a chitin derivative containing hydroxyl and amino functional groups, has attracted significant interest owing to its cost-effectiveness, general availability, non-toxicity, biocompatibility, and biodegradability.[19] CS contains numerous hydroxyl groups and glucosamine and has high reactivity. Its properties can be tailored using various modification methods.[20,21] However, its high solubility, mechanical properties and swelling rate in acid media pose challenges to its application in environmental remediation, making it difficult to use CS in batches and, especially, in large fixed-bed column operations.[22] Alginates are particularly interesting as structural composites because of their exceptional stability and biodegradability. The hydroxyl (–OH) and carboxyl (–COO) groups in alginates provide unique coordination sites for the adsorption of dyes and heavy metal ions in wastewater.[23] Recently, the incorporation of natural macromolecules into the network of adsorbent polymers has proven to be an effective method for developing materials with unique properties.[24,25] Chitosan–alginate complexes have attracted increasing attention for their potential in environmental remediation applications.[26] However, pure natural polymers suffer from a low surface area, low flexibility and high water-solubility. However, desirable properties, such as increased mechanical strength, heat resistance, chemical

School of Chemistry and Environmental Engineering, Wuhan Polytechnic University, Wuhan 430023, PR China. E-mail: zhanglei@whpu.edu.cn; huangyj@whpu.edu.cn

† Electronic supplementary information (ESI) available. See DOI: https://doi.org/10.1039/d5ra00940e

resistance and water adsorption, can be achieved by making structural changes to the materials, such as adjusting their specific surface areas, changing their pore dimensions and incorporating functional groups.[27,28] Because some currently used materials are undesirable, chemical modification can help improve their performance through the introduction of specific functional groups that would aid in the removal of heavy metal ions and dye molecules.[29,30] Ethylenediaminetetraacetic acid (EDTA) is a chelating agent known for its strong complexing properties, which may endow adsorbents with an excellent metal-binding ability through multiple hydrogen bond interactions with target pollutants through coordination and chelation.[31] Sun *et al.* prepared EDTA-modified magnetic attapulgite–chitosan gel beads for the removal of Pb(II), Cu(II), and Ni(II), with maximum adsorption capacities of 368.32, 267.94, and 220.31 mg g^{-1}, respectively. Moreover, even after five cycles of reuse, the beads demonstrated excellent adsorption performance, broad pH applicability, and the ability to achieve the rapid separation of the heavy metals.[32] However, the chemical crosslinking traditionally used to prepare CS gel reduces the number of active sites for heavy metal ions and dyes and leads to the formation of a dense molecular structure, resulting in a decrease in the adsorption capacity of chitosan and a slower adsorption rate.[33] Zhang *et al.* successfully prepared a calcium alginate-based porous nanocomposite hydrogel (CPGA) using $CaCO_3$ as a pore-forming agent to enhance its performance for removing Cu(II) from water. Experimental results demonstrated that the maximum adsorption capacity of CPGA for Cu(II) reached 291.2 mg g^{-1}. Furthermore, the CPGA exhibited excellent anti-interference capabilities in the presence of sodium chloride and humic acid, as well as in real Cu(II)-contaminated lake water environments.[34]

To address these shortcomings, a novel EDTA-chitosan/alginate porous composite bead is proposed in this paper, which can improve the ability of the adsorbent to capture heavy metal ions and dyes as well as improve the adsorption capacity and separation performance. Investigations were carried out on the structure, adsorption properties and mechanism of the enhanced porous composite beads, and the simultaneous removal of the heavy metal ions Pb(II) and MB from aqueous solution by the adsorbent was studied in detail. This study also compared the adsorption capacity of our chitosan-based adsorbent toward Pb(II) and MB with that of some previously reported systems.[35–37] According to experimental results, the as-prepared adsorbent exhibited high adsorption performance toward Pb(II) and MB and could maintain good performance after its regeneration, highlighting its potential application for the simultaneous removal of Pb(II) and MB dye contaminants from wastewater.

2. Materials and methods

2.1 Materials

1-Ethyl-3-(3-dimethylaminopropyl) carbodiimide hydrochloride (EDAC, 98%), chitosan (CS, deacetylation ≥95%, viscosity of 100–200 mPa s) and sodium alginate (ALG, viscosity of 200 ± 20 mPa s) were acquired from Shanghai Aladdin Chemical Reagent Co., Ltd (China). $CaCO_3$ (AR), ethylenediaminetetraacetic acid (EDTA, AR), $Pb(NO_3)_2$ (AR), methylene blue (MB, AR) and glutaraldehyde (GLA, BR, 25 wt%) were supplied from Sinopharm Chemical Reagent Co., Ltd (China). All experiments were performed using deionized (DI) water.

2.2 Synthesis of EDTA-modified chitosan (EDCS)

EDCS polymers were synthesized according to a previously reported method.[38] First, 2.0 g of CS, 3.6 g of EDTA and 0.72 g NaOH were dispersed in 100 mL of demineralized water, and stirred until the chitosan and EDTA were completely dissolved. Afterwards, 9.5 g of EDAC was dissolved in 40 mL of ice water and then mixed into the dispersion medium, and then placed in an ice bath for 6 h with stirring. Afterwards, the residue was washed successively with 0.1 M NaOH and deionized water, and then with 0.1 M HCl and deionized water, until the pH of the rinsing water wash-off approached neutral. After filtration, EDTA-modified chitosan was obtained, which was denoted by the abbreviation EDCS.

2.3 Preparation of porous EDTA-chitosan/alginate composite beads (EC–AB)

First, 0.25 g EDCS was mixed in 10 mL of 1.25 wt% sodium alginate solution. Then a certain amount of $CaCO_3$ (0–0.5 g) was added in the dispersion medium and mechanically stirred for 12 h to form a homogeneous suspension. The homogeneous suspension was successively added dropwise into a 0.15% $CaCl_2$ solution and transferred to an acetic acid (HAc) solution to remove residual $CaCO_3$. The beads not crosslinked with GLA and containing 0% $CaCO_3$ were denoted as ECB. The beads containing $CaCO_3$ were subsequently crosslinked with 1 wt% GLA solution and labeled EC–AB. After 12 h, the obtained beads were filtered and washed with deionized water to removal any unreacted substances. Afterwards, these beads were kept in deionized water. The process diagram for preparing the EC–AB spherical beads is shown in Scheme 1.

2.4 Characterizations

Fourier transform infrared (FTIR) analysis was performed using an FTIR spectrometer (Thermo Scientific Nicolet Is 10, USA). The surface morphologies and distribution of elements in the samples were determined using field emission scanning electron microscopy (SEM, ZEISS Gemini 300, Germany), equipped with an energy dispersive X-ray (EDS) analyzer. The zeta potential of EC–AB was measured at different pH values (1–10) using BENANO 180 ZATE PRO. The concentration of Pb(II) was analyzed through atomic adsorption spectroscopy (AAS, icE 3000 Series, Thermo Fisher Scientific, USA). The dye concentration was estimated through photometric spectrophotometry (Beijing Puxi T6, China) using a UV-vis spectrophotometer to monitor the absorbance at $\lambda_{max} = 664$ nm.

2.5 Batch adsorption experiments

The Pb(II) (1000 mg L^{-1}) and MB (10 000 mg L^{-1}) solutions were prepared and used for all batch adsorption experiments. Furthermore, all the experiments were performed by taking

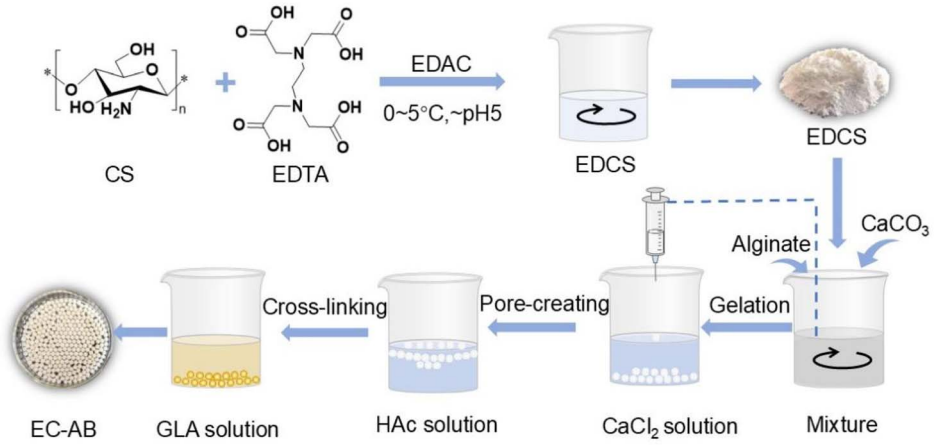

Scheme 1 Schematic of the preparation of EC–AB.

a mixture of 10 mg adsorbent with 10 mL wastewater in 15 mL centrifuge tubes, followed by placing them on a thermostatic oscillator at 25 °C with a 175 rpm oscillation frequency. The pH effect was examined in the range of 1–6 for Pb(II) and 2–10 for MB with initial concentrations of 300 and 500 mg L^{-1}, respectively, with a contact time 24 h. To adjust the pH of the solution, 0.1 mol per L NaOH/HNO_3 was used for Pb(II) and 0.1 mol per L NaOH/HCl for MB. Adsorption kinetics tests were performed with Pb(II) and MB at initial concentrations of 300 and 500 mg L^{-1}, with time intervals of 20–2280 and 30–2280 min, respectively, at pH 6. Adsorption isotherms were investigated at pH 6 with Pb(II) and MB at concentrations of 15–1000 and 20–3000 mg L^{-1}, respectively. For investigating the effect of interfering ions, $Na^+/Mg^{2+}/Ca^{2+}/Cl^-/NO_3^-/SO_4^{2-}$ were added to the solutions at varying concentrations of 0, 10, 50, and 100 mmol L^{-1}. After each experiment, the sorbents were removed from the solutions using 0.45 μm polypropylene spray filters. After dilution with 2% HNO_3, the Pb(II) concentration was measured using atomic adsorption spectrometry. The concentration of the MB solution was measured using a UV-vis spectrometry.

2.6 Fixed-bed column studies

Fixed-bed tests were conducted using a glass pillar (20 cm length and 0.7 cm diameter), filled with 0.5 g of adsorbent (dry weight, and a bed height of 18 cm). The pollutant solutions containing 25 mg L^{-1} of Pb(II) or MB were passed through the column at a flow rate of 1.5 mL min^{-1}. The effluents were collected at regular intervals and the concentration of residual contaminants (C_t) was analyzed. The outlet Pb(II) and MB effluent solutions were sampled regularly up to the saturation point at $C_t/C_0 = 0.95$, in which C_0 (mg L^{-1}) and C_t (mg L^{-1}) represent the inlet and outlet concentrations of Pb(II) and MB, respectively. The adsorption behavior of EC–AB for Pb(II) and MB in the fixed-bed reactor was described by the breakthrough point of the curve of C_t/C_0 plotted against time.

2.7 Evaluation of EC–AB performance in a binary system

To explore the efficiency of EC–AB in the simultaneous removal of Pb(II) and MB and the mutual effects between them in complex wastewater, the adsorption capacity of the EC–AB composite for the individual pollutants in a binary system was studied and compared with the adsorption capacities of single-pollutant systems. Batch adsorption experiments were performed using a concentration range of 0–300 mg L^{-1} for Pb(II) and 0–500 mg L^{-1} for MB. In the binary system, the experiments were performed under the same conditions as those for the single sorption system with an initial pH of 6.0 and contact time of 24 h.

All the experiments were carried out in triplicate and the mean values were used to analyze the data. The adsorption capacity (q_e, mg g^{-1}) as well as the removal efficiency (R, %) of the adsorbent were determined using eqn (1) and (2), respectively:

$$q_e = \frac{(C_0 - C_e)}{m} \times V \quad (1)$$

$$R = \frac{(C_0 - C_e)}{C_0} \times 100\%, \quad (2)$$

where q_e (mg g^{-1}) is the equilibrium adsorption capacity of EC–AB, C_0 (mg L^{-1}) and C_e (mg L^{-1}) denote the initial and equilibrium concentrations of the Pb(II) or MB solution, respectively, m (g) stands for the mass of the adsorbent, and V (L) represents of the volume of the Pb(II) or MB solution.

2.8 Regeneration studies

Five consecutive adsorption and regeneration cycles were performed to assess the reusability of EC–AB. Initially, 30 mg of EC–AB was added to separate 30 mL solutions containing 300 mg L^{-1} of Pb(II) or 500 mg L^{-1} MB solution in 50 mL centrifuge tubes. After achieving equilibrium, Pb(II)-loaded and MB-loaded EC–AB was recovered. Pb(II) ions were eluted using an acidified thiourea solution (0.1 M HNO_3 + 4% thiourea), while MB was desorbed using acidified ethanol (5% HCl with ethanol). EC–AB was subsequently rinsed with deionized water to neutralize it so that it could be reused in subsequent cycles. These steps were repeated five times, and the reusability of EC–AB was evaluated based on the experimental outcomes. The

regeneration efficiency (RE, %) of EC–AB was calculated as follows:

$$\mathrm{RE} = \frac{q_r}{q_0} \times 100\%, \quad (3)$$

where q_0 and q_r are the adsorption capacities of EC–AB (mg g^{-1}) before and after its regeneration, respectively.

3. Results and discussion

3.1 Characterization

Fig. 1 presents the FTIR spectra of CS, EDCS, ALG, ECB, and $CaCO_3$-3wt% crosslinked beads (EC–AB). The CS adsorption peak observed at 3440 cm^{-1} was due to N–H and O–H stretching vibrations, while the two peaks at 2921 and 2877 cm^{-1} were related to the symmetric and asymmetric stretching vibrations of aliphatic $-CH_2$, respectively.[39] The peaks around 1653, 1601 and 1384 cm^{-1} were attributed to the vibrations of amide I and amide II and CH_3 symmetrical angular deformation, respectively.[40,41] Furthermore, bands for the CS polysaccharide backbone were observed in the range of 1156–897 cm^{-1}. Compared with CS, the evident enhanced adsorption peaks of EDCS at 1635 and 1585 cm^{-1} were assigned to the C=O stretching vibrations of $-COO^-$ and –NH bending vibration of the amide groups, respectively.[42,43] Moreover, The characteristic bands at 1399 and 1069 cm^{-1} corresponded to the C–O and C–C stretching vibration in $-COO^-$ groups. All these bands confirmed the functionalization of CS with EDTA through amide bonds and verified that the carboxyl group in EDTA was successfully introduced into EDCS.[44] Sodium alginate (ALG) has characteristic bands for hydroxyl at 3430 cm^{-1}, C–H stretching vibrations at 2929 cm^{-1}, carboxyl at 1614 and 1416 cm^{-1}, and carbonyl at 1032 cm^{-1}.[45] By combining with ALG, porous beads could be prepared without sacrificing the carboxyl groups. The enhanced absorption peak at 1634 cm^{-1} represented carbonyl stretching vibration of the amide bonds, while the new peak observed around 1420 cm^{-1} was attributed to the interaction between the $-NH_3^+$ groups of chitosan and the $-COO^-$ groups of the alginate.[46] In the case of the EC–AB spectrum, the enhanced absorption peak at 1652 cm^{-1} was related to the C=O stretching vibration from the amide bonds and carboxylic groups,[31] while the peak at 1589 cm^{-1} was related to the bending vibration of the N–H amide.[47] Also, the peaks at 1039 and 1157 cm^{-1} matched with the antisymmetric vibrations (C–O–C), indicating that the –CHO of glutaraldehyde had reacted with the –OH of chitosan and the alginate.[48]

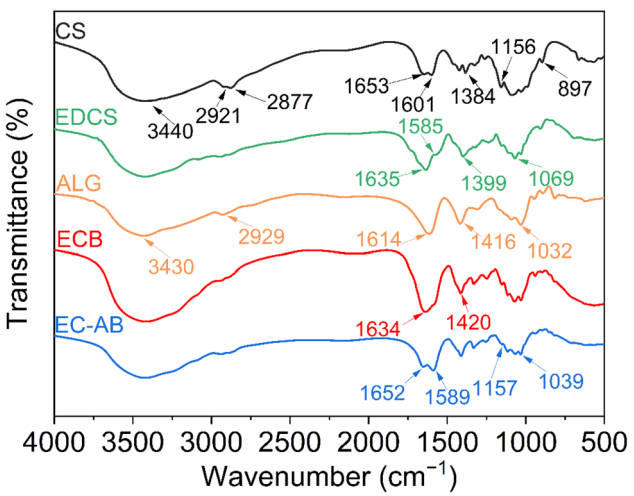

Fig. 1 FTIR spectra of CS, EDCS, ALG, ECB and EC–AB.

The structural characteristics of the 3 wt% $CaCO_3$-containing crosslinked beads (EC–AB) are given in Fig. 2A–D. It can be seen that EC–AB is a typical spherical particle with a rough and fragmented surface and a porous structure, with a diameter of around 1 mm. Next, EDS mapping was employed to identify the composition of the prepared EC–AB beads, and the results are presented in Fig. 2E. The mapping of the obtained EC–AB showed a homogenous distribution of C, N, O and Ca, with their atomic ratios given in Table S2† (C: 53.22%, N: 3.69%, O: 36.9%, and Ca: 8.71%).

The nitrogen adsorption–desorption isotherms of EC–AB and ECB are presented in Fig. S1,† with their structural parameters listed in Table 1. EC–AB exhibited a BET surface area of 27.9 m^2 g^{-1}, which is significantly higher than that of ECB (18.5 m^2 g^{-1}), demonstrating that $CaCO_3$ incorporation effectively increased the specific surface area of the chitosan beads. Additionally, EC–AB displayed a larger pore size (0.051 nm) than that of ECB. Type IV adsorption–desorption isotherms further confirm the mesoporous nature of both adsorbents, which enhances mass transfer during the adsorption of metal ions and dyes.

3.2 Single pollutant system adsorption studies

3.2.1 Effect of the $CaCO_3$ dosage. The amount of $CaCO_3$ added significantly influenced the number of functional groups adsorption sites in EC–AB, thus affecting its adsorption performance. Fig. 3 displays the adsorption capacities of EC–AB with varying the $CaCO_3$ addition for Pb(II) and MB. It can be seen that the ability of EC–AB to adsorb Pb(II) or MB gradually became more effective as the $CaCO_3$ content was increased, and the samples with 3% $CaCO_3$ addition had better adsorption capacity for Pb(II) and MB than the lower concentration $CaCO_3$ additions. Meanwhile, the adsorption capacity of EC–AB remained unchanged when the $CaCO_3$ addition amount was above 3%. However, excessive $CaCO_3$ addition reduced the material stability. Therefore, 3% $CaCO_3$ addition in the EC–AB samples was chosen as the optimal condition for the subsequent tests. The improved adsorption performance with $CaCO_3$ addition could be attributed to several factors: (1) $CaCO_3$ acted as a pore-forming agent, which enhanced the specific porous surface area of the hydrogels; (2) due to the products of the solubility of $CaCO_3$ (3.36×10^{-9}) and $PbCO_3$ (7.4×10^{-14}), the residual $CaCO_3$ provided cation exchange reaction sites, enhancing the scavenging of Pb(II).

3.2.2 Effect of pH. The initial pH of the aqueous solution changed the surface charge state of the adsorbent, influencing the interaction between Pb(II) ions, MB, and the active sites on the EC–AB surface.[49] Fig. 4A shows the effect of pH on the

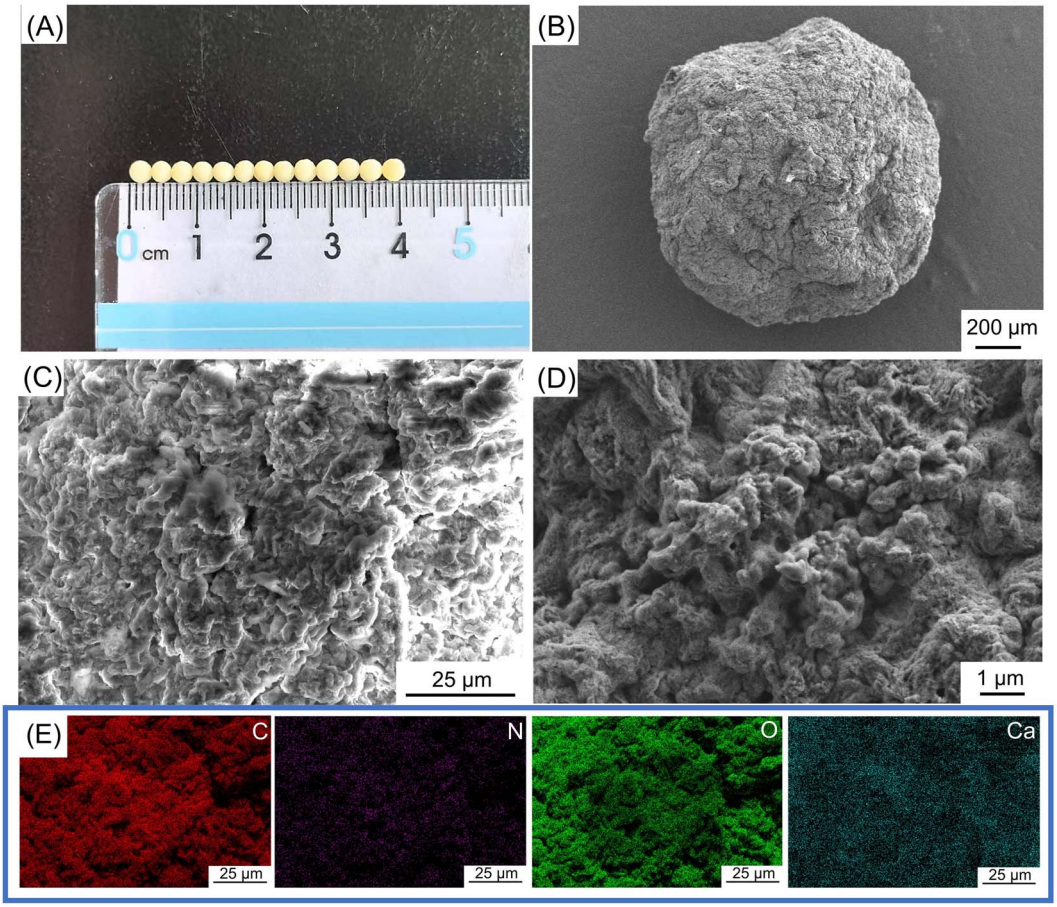

Fig. 2 (A) Digital photograph of EC–AB, (B–D) SEM images of EC–AB and (E) elemental mapping as analyzed using EDS.

Table 1 Structural parameters of EC–AB and ECB

Samples	Specific surface area (m^2 g^{-1})	Volume of pores (cm^3 g^{-1})	Average pore size (nm)
EC–AB	27.9	0.057	0.051
ECB	18.5	0.047	0.043

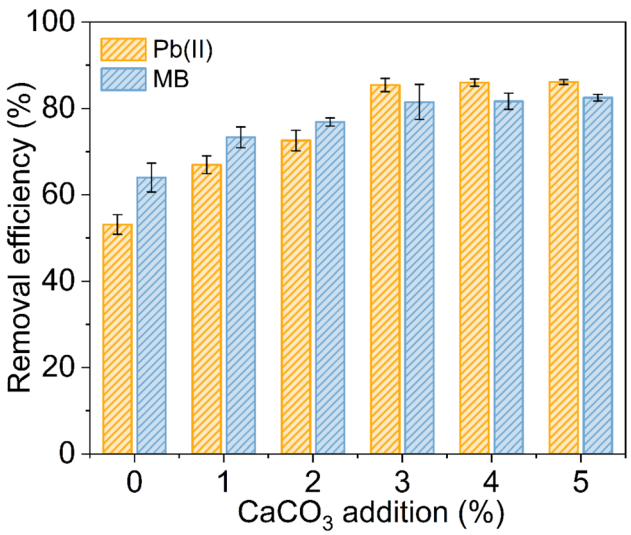

Fig. 3 Effect of the addition of $CaCO_3$ on Pb(II)/MB adsorption.

removal efficiency of EC–AB toward Pb(II) or MB. The pH range investigated was set below 6 for Pb(II) and 10 for MB to avoid metal hydroxide precipitation and MB decomposition under alkaline conditions.[50] The results showed that the removal efficiency of Pb(II) and MB initially increased with an increase in solution pH and then remained constant. EC–AB had a low point of zero charge (pH_{pzc}) of 2.01, as shown in Fig. 4B, and its removal efficiency toward Pb(II) and MB depended on the electrostatic interactions between the adsorbent and pollutants. At lower pH ($<pH_{pzc}$), the EC–AB polymer surface became positively charged with protons, leading to a decrease in adsorption capacity owing to electrostatic repulsion. With an increase in the pH value of the solution, the EC–AB surface became negatively charged owing to proton removal and the electrostatic attractions between opposite ions with charge ions, thus promoting Pb(II) and MB removal. Furthermore, at a lower pH, a decrease in removal efficiency was observed owing to competition between the positively charged pollutants and a large amount of H^+ or H_3O^+ in the solution.[31,51] As the pH of the solution was increased, chelates were more easily formed

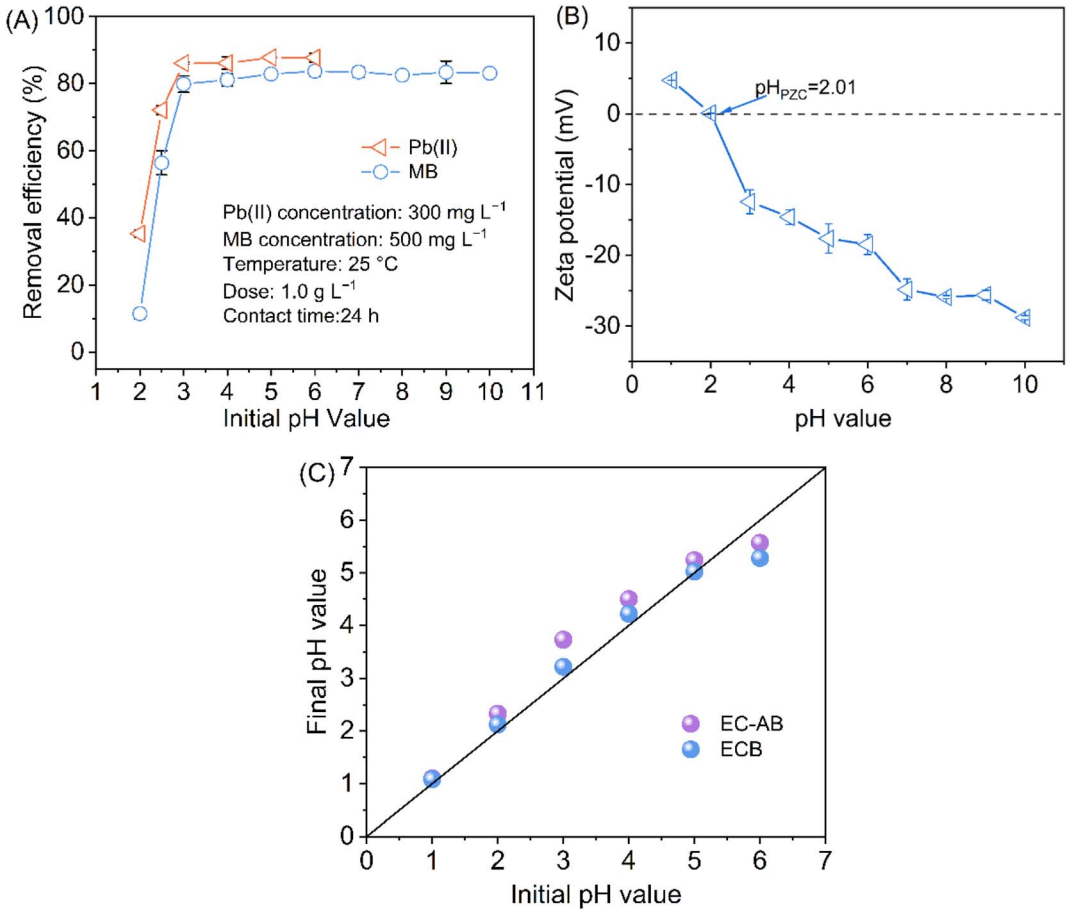

Fig. 4 (A) Effect of the initial pH on the Pb(II)/MB removal efficiency of EC–AB. (B) Zeta potential and (C) comparison of the pH values of EC–AB and ECB solutions before and after 24 h of storage in different pH solutions.

between Pb(II) and the nitrogen atom of CS, owing to the increased deprotonation of the amino groups in CS. The electrostatic interaction between the negatively charged COO^- groups of EDTA and the heavy metals dominated the adsorption process.[52,53] Thus, these two adsorption mechanisms synergistically increased the adsorption capability of EC–AB toward Pb(II). In MB adsorption, the high adsorption capacity was probably achieved owing to the electrostatic interactions between EDTA groups and MB. Moreover, the H^+ groups of –COOH on EDTA could be relocated to the nitrogen atom of the amino groups and form negatively charged sites, which also participated in MB adsorption in the aqueous solution.

Fig. 4C shows the variation in the solution pH before and after EC–AB material immersion across different initial pH conditions. Within the initial pH range of 1–6, the post-immersion pH increased by 0.1–0.5 units, indicating that the residual $CaCO_3$ functioned as a pH stabilizing agent for adsorption, which indirectly improved the adsorption efficiency.[54]

3.2.3 Effect of the contact time and adsorption kinetics. Fig. 5 shows the temporal relationship with the adsorption amount of the two pollutants, with both showing similar trends. Both pollutants initially underwent a rapid adsorption and then gradually achieved equilibrium over time. This phenomenon can be explained by the large number of functional groups on the surface of the EC–AB adsorbent during the initial stages, with ample adsorbent sites.[22] Additionally, the surface of the EC–AB adsorbent exhibited a high density of negative charges, and therefore enhanced electrostatic attraction for Pb(II) adsorption. As the adsorption sites deceased in the later stages, the EC–AB surface became increasingly occupied by pollutants, leading to a saturation point, whereby the adsorption rates gradually diminished until equilibrium was achieved.

Next, three widely used kinetic models—the pseudo-first-order model (4),[55] pseudo-second-order model (5) (ref. 56) and intra-particle diffusion model (6)—[57] were used to evaluate the kinetic adsorption mechanism of Pb(II) and MB on EC–AB, which can be expressed as follows:

Pseudo-first-order model:

$$q_t = q_e(1 - \exp^{-k_1 t}) \quad (4)$$

Pseudo-second-order model:

$$q_t = \frac{q_e^2 k_2 t}{1 + k_2 q_e t} \quad (5)$$

Intra-particle diffusion model:

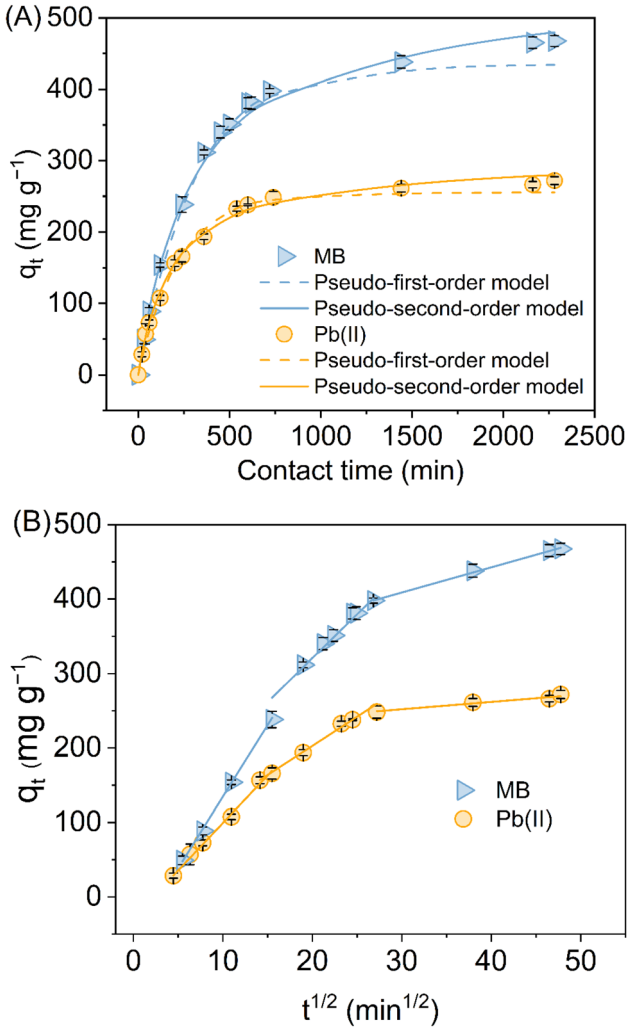

Fig. 5 (A) Adsorption kinetics of Pb(II)/MB on EC–AB (pseudo-first-order and pseudo-second-order kinetic model fitting); (B) intra-particle diffusion fitting.

$$q_t = k_i t^{1/2} + C, \tag{6}$$

where q_t (mg g^{-1}) and q_e (mg g^{-1}) are the adsorption capacity of adsorbents at time t (min) and at the steady state, respectively; k_1 (min^{-1}) and k_2 (g mg^{-1} min^{-1}) are the rate constants for the pseudo-first-order and pseudo-second-order models, respectively; k_i (mg g^{-1} min$^{-1/2}$) is the rate constant of intra-particle diffusion and C_i (mg g^{-1}) is the boundary layer thickness coefficient.

Furthermore, the root mean square error (RMSE) was utilized to evaluate the value variance between the experimental data and the predicted values. Generally, the lower the RMSE value, the better the fit of the corresponding kinetic model. The RMSE value was determined using the equation below:

$$\mathrm{RMSE} = \sqrt{\frac{1}{n}\sum_{i=1}^{n}\left(q_{\mathrm{cal}_i} - q_{\mathrm{exp}_i}\right)^2} \tag{7}$$

Fig. 5 presents the fitting diagrams of the pseudo-first-order and pseudo-second-order kinetic models as well as the intra-particle diffusion models used for the EC–AB adsorbent for Pb(II) and MB removal. The corresponding kinetics parameters are listed in Table 2. In contrast, the RMSE value of the pseudo-second-order dynamic adsorption model for EC–AB was lower than that of the pseudo-first-order model, indicating a better fit and implying that the adsorption of Pb(II) and MB followed a chemical adsorption process, such as ion exchange, surface complexation, and/or precipitation.[58,59]

Furthermore, the intra-particle diffusion models were integrated into the fitting process to investigate the rate-limiting steps between EC–AB and Pb(II)/MB, providing more in-depth insights into the adsorption mechanism. As illustrated in Fig. 5B, the plots for EC–AB did not exhibit linear relationships intersecting the origin, implying that intra-particle diffusion was not the sole rate-determining step. The adsorption process of EC–AB was divided into three stages: (i) an initial boundary diffusion, during which a significant amount of Pb(II)/MB rapidly occupies the functional sites on the EC–AB surface; (ii) followed by intra-particle stages and (iii) progressive diffusion from the outer surface to the inner framework of EC–AB, ultimately achieving adsorption equilibrium. The slopes obtained from data fitting demonstrated the hierarchy of rate constants as $k_{i,1} > k_{i,2} > k_{i,3}$, revealing that surface boundary diffusion governs the rate-controlling step.

3.2.4 Adsorption isotherms. Fig. 6 shows the trend for the adsorption isotherms, wherein the initial concentration of Pb(II) and MB affected the adsorption capacities of EC–AB, which initially increased before reaching equilibrium. The observation that the adsorption rate was very fast in the initial stage was ascribed to the abundance of available adsorption sites and the essential concentration gradient between the pollutants and the adsorbent at the solid–liquid interface.[60] However, given the fixed amount of the adsorbent, the quantity of accessible binding sites remained limited. Once the contaminant level exceeded a critical threshold, all adsorption sites became occupied, resulting in adsorption equilibrium. These findings underscore how concentration gradients influence mass-transfer dynamics and drive adsorption processes in high-concentration heavy metal scenarios.[61]

Conventional Langmuir and Freundlich isotherm models were used to estimate the maximum adsorption capacity and adsorption properties in the interactions between EC–AB and Pb(II) and MB. The non-linear properties of the two isotherm models were as follows:

Langmuir isotherm model:

$$q_e = \frac{q_m K_L C_e}{1 + K_L C_e} \tag{8}$$

Freundlich isotherm model:

$$q_e = K_F C_e^{1/n_F}, \tag{9}$$

where q_m (mg g^{-1}) represents the maximum adsorption capacity of the EC–AB adsorbent, K_L (L mg^{-1}) is the Langmuir equilibrium constant, and K_F (mg$^{(1-n)}$ L^n g^{-1}) and n_F are the

Table 2 Kinetics parameters for the adsorption of Pb(II) and MB by EC–AB

		Adsorbent	
Kinetic models	Parameters	Pb(II)	MB
Pseudo-first-order model	$q_{e,exp}$ (mg g^{-1})	271.80	467.35
	$q_{e,cal}$ (mg g^{-1})	255.15	434.05
	k_1 (min^{-1})	0.0046	0.0033
	RMSE	8.86	14.45
	R^2	0.9954	0.9970
Pseudo-second-order model	$q_{e,cal}$ (mg g^{-1})	279.76	540.08
	k_2 (g mg^{-1} min^{-1})	0.000018	0.0000017
	RMSE	6.05	10.26
	R^2	0.9978	0.9975
Intra-particle diffusion model	$k_{i,1}$ (mg g^{-1} min$^{-1/2}$)	12.74	19.24
	$k_{i,2}$ (mg g^{-1} min$^{-1/2}$)	7.83	11.75
	$k_{i,3}$ (mg g^{-1} min$^{-1/2}$)	0.99	3.39
	$C_{i,1}$ (mg g^{-1})	−28.18	−57.60
	$C_{i,2}$ (mg g^{-1})	46.13	85.57
	$C_{i,3}$ (mg g^{-1})	222.42	307.03

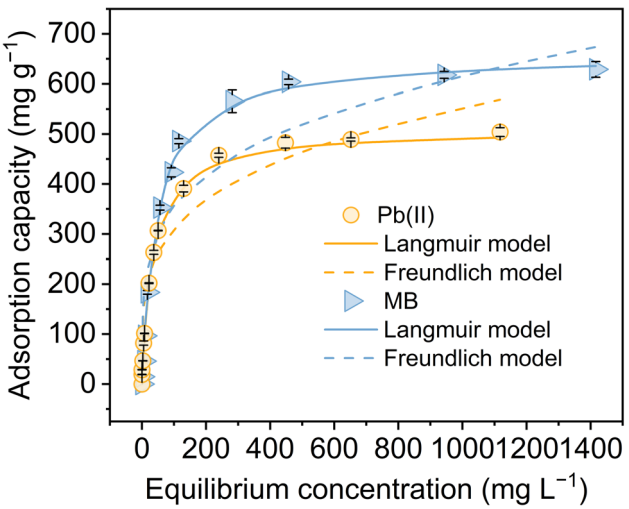

Fig. 6 Adsorption isotherms of Pb(II)/MB on EC–AB.

Freundlich constant related to the adsorption capacity of the EC–AB adsorbent and the heterogeneity factor, respectively.

An overview of the isotherm parameters and RMSE values is provided in Table 3. The Langmuir isotherm model was selected to characterize the adsorption behavior of EC–AB owing to its lower RMSE values compared with the Freundlich model,

Table 3 Isotherm parameters of Pb(II) and MB adsorption on EC–AB

		Adsorbent	
Kinetic models	Parameters	Pb(II)	MB
Langmuir model	$q_{m,exp}$ (mg g^{-1})	504.11	660.76
	$q_{m,cal}$ (mg g^{-1})	492.97	655.97
	K_L (L mg^{-1})	0.03	0.022
	RMSE	13.01	14.07
Freundlich model	n_F	4.07	4.18
	K_F ((mg g^{-1})/(mg L^{-1})$^{1/n}$)	101.29	118.83
	RMSE	47.67	90.34

indicating its preference for homogeneous monolayer chemisorption on the adsorbent surface. Table 4 compares the adsorption capacities of EC–AB with those of previously reported chitosan adsorbents for Pb(II) and MB. It is evident that the EC–AB composite in this study demonstrated superior adsorption capacity compared with most of the reported adsorbents.

3.2.5 Effects of interfering ions. Generally, wastewater contains various coexisting anions and cations that can affect the adsorption efficiencies for Pb(II) and MB through competitive binding. Therefore, the adsorption efficiency of EC–AB for Pb(II) and MB in solutions with coexisting anions and cations at different concentrations was studied, and the results are shown in Fig. 7. It was found that the adsorption capacities of Pb(II) were not substantially affected by varying concentrations of Na^+, Mg^{2+}, Cl^-, and NO_3^-. However, as the concentrations of Ca^{2+} and sulfate (SO_4^{2-}) increased, the adsorption capacities of Pb(II) gradually decreased. Thus, the presence of coexisting cations and anions could significantly inhibit the removal efficiency of MB. The presence of cations reduces the adsorption efficiency when electrostatic interactions exist between the adsorbent and contaminants.[68,69] This indicates that electrostatic attraction plays a predominant role in the uptake of MB by the positively charged EC–AB adsorbent.

The negative impact of ionic strength on the adsorption efficiency could be ascribed to two factors. Firstly, increasing the ionic strength compresses the electrical double layers of the adsorbent, thereby suppressing the electrostatic attraction between the EC–AB adsorbent and adsorbates. Secondly, the introduction of co-existing anions and cations competes with Pb(II) and MB molecules for cationic sites on the EC–AB adsorbent surface, ultimately reducing the adsorption of Pb(II) and MB molecules onto EC–AB.[70]

3.3 Simultaneous adsorption studies of the binary system

The influence of the binary system on the adsorption of contaminants was investigated using mixed solutions with

Table 4 Comparison of the adsorption performance of chitosan-based adsorbents toward Pb(II) and MB

Adsorbent	Adsorption efficiency q_m (mg g^{-1})		Tem.	pH	References
	Pb(II)	MB			
EC–AB	504.11	660.76	25 °C	6	This work
Fe_3O_4-CS/EDTA	220.0	459.9	30 °C	6/10	35
CS/EDTA/CBC	1105.78	590.72	25 °C	6/7	36
FFO@Sil@Chi-DTPA	259.45	546.73	45 °C	6	37
β-CD-EDTA-CS	—	107.20	20 °C	8.3	62
NTA-β-CD-CS	—	162.6	22–25 °C	6	63
MGO@TETA@MACS	—	247.37	25 °C	8	64
DOTA@sludge@chitosan	329.4	—	20 °C	5.08	61
CS-PDA aerogel	441.2	—	—	5.5	65
Thermosensitive CS/Pec	97.55	—	25 °C	4	66
CS-PAA	204.89	—	—	6	67

varying initial concentration of Pb(II) and MB. The adsorption capacity of EC–AB in the presence of Pb(II) and MB within the binary system was evaluated by the adsorption capacity ratio (R) as follows:

$$R_q = \frac{q_{b,i}}{q_{m,i}} \quad (10)$$

where $q_{b,i}$ and $q_{m,i}$ represent the equilibrium adsorption of contaminant i in the binary or in the single-component system at an identical initial concentration, respectively. The previous literature suggested that: if $R_q > 1$, the sorption of contaminant was enhanced by the co-pollutant; if $R_q = 1$, the co-pollutant did not influence the adsorption of the pollutant; and if $R_q < 1$, the adsorption of the pollutant was inhibited by the co-pollutant.[71]

Fig. 8 shows the Q_e (Fig. 8A and C) and R_Q (Fig. 8B and D) results across different starting concentrations within the mixed-component system. It can be seen that the adsorption of Pb(II) remained nearly unchanged ($R_{Q,Pb(II)} \approx 1$) at low initial Pb(II) levels (100 and 200 mg L^{-1}) in the presence of MB. Notably, an enhanced capacity of Pb(II) ($R_{Q,Pb(II)} > 1.0$) was observed in the presence of high MB concentrations (300, 400 and 500 mg L^{-1}). Thus, the presence of MB not only did not negatively impact Pb(II) adsorption but actually enhanced it at higher Pb(II) concentrations. This synergistic effect may be due to the presence of MB on the EC–AB surface through EDTA inclusion complexation, potentially creating new adsorption sites for Pb(II) ions.[72]

Similarly, MB adsorption ($R_{Q,MB} \approx 1$) onto EC–AB was unaffected by the low initial Pb(II) concentration (50 mg L^{-1}). In comparison with the behavior of Pb(II) uptake, the sorption of MB ($R_{Q,MB} < 1$) was markedly decreased at comparatively high Pb(II) levels (100 mg L^{-1}), indicating an inhibitory effect of Pb(II) on MB adsorption within the dual-component system.[62] Moreover, this negative effect increased with increasing the MB concentration, suggesting that more MB particles were displaced from their original adsorption sites. These results may be due to the following reasons: (1) there was competitive adsorption between the positively charged MB and positively charged Pb(II). Generally speaking, the stronger the electronegativity, the easier it is for a material to be adsorbed by the adsorbent. The order of electronegativity of the two pollutants was Pb(II) > MB.[36] Therefore, in comparison to MB, it is easier for Pb(II) to approach the surface of the adsorbent and participate in reactions;[62] (2) there was a steric hindrance effect at the pores

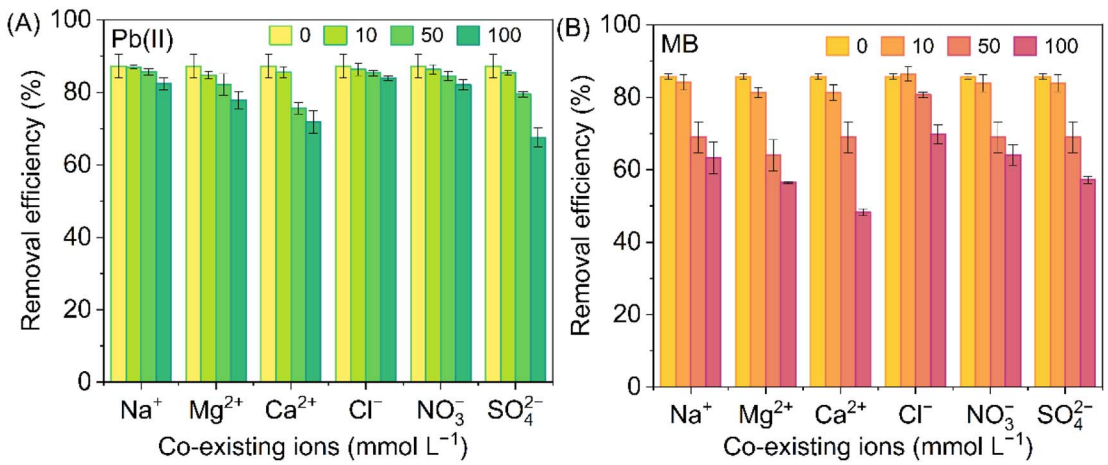

Fig. 7 Effect of co-existing ions on the removal efficiencies of Pb(II) (A) and MB (B).

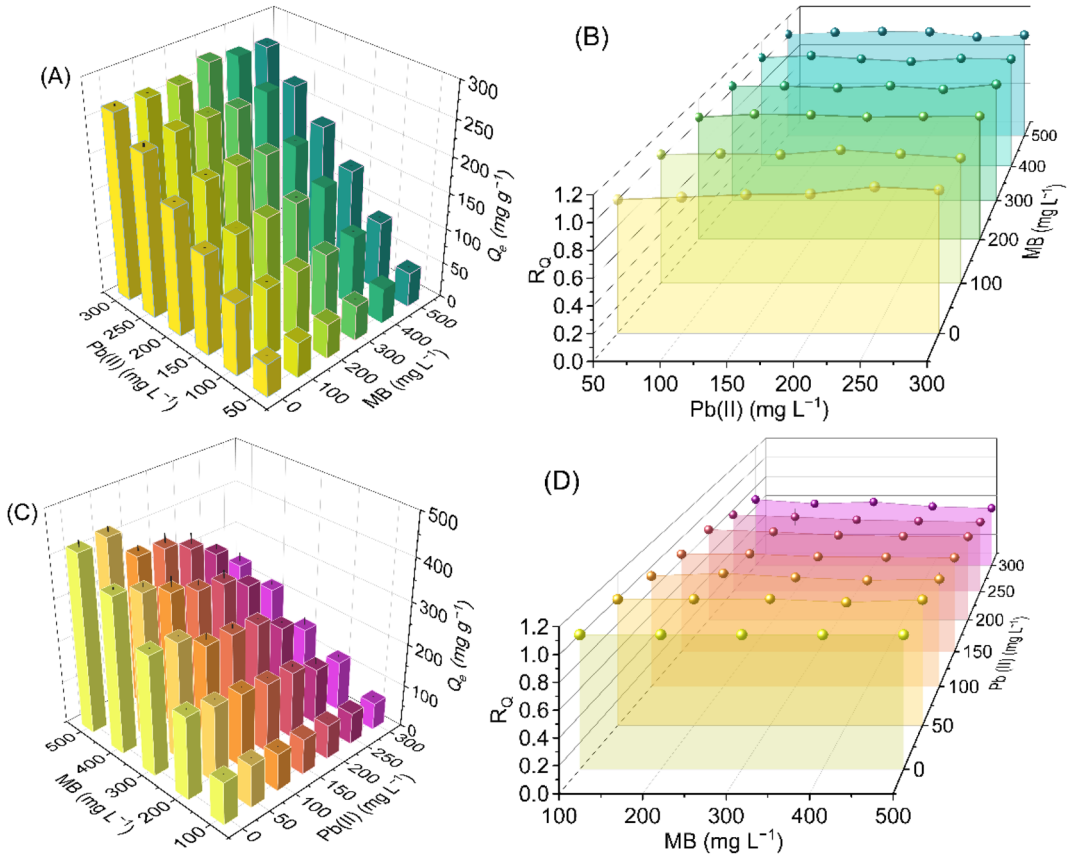

Fig. 8 Q_e and R_Q values *versus* the initial concentrations of Pb(II) and MB in the binary system for the simultaneous adsorption of Pb(II) (A and B) and MB (C and D).

surrounding the dense complex formed by Pb(II) and oxygen-containing groups (–OH and –COOH/–COO–) with the increasing Pb(II) concentration.[73]

3.4 Fixed-bed column data

To assess the applicability of the immobilized EC–AB adsorbent for real wastewater treatment, a continuous treatment reactor was employed for assessing Pb(II) and MB removal. The characteristics of this adsorbent were determined through plotting the breakthrough curves in fixed-bed columns. As shown in Fig. 9, the breakthrough curves exhibited a characteristic S-shape outline. Approximately 0.05 of Pb(II) was adsorbed in 120 min, marking the breakthrough time (t_b). Subsequently, the Pb(II) concentration rose sharply until the column achieved

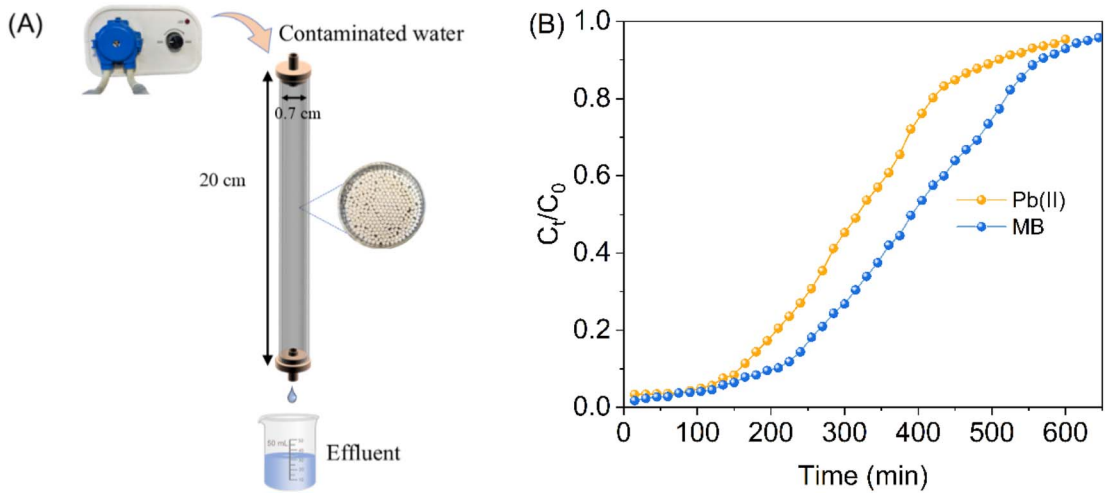

Fig. 9 (A) Schematic of the adsorption fixed-bed mini-column. (B) Adsorption breakthrough curves for Pb(II) and MB.

equilibrium at approximately 585 min, which was considered as the exhaustion time (t_e), indicating an adsorption efficiency of only 0.95 for Pb(II). Similarly, for MB, the breakthrough point ($C_t/C_0 = 0.05$) and exhaustion point ($C_t/C_0 = 0.95$) occurred at approximately 200 and 650 min, respectively. The breakthrough capacities were 20.92 and 20.41 mg g^{-1} for Pb(II) and MB, respectively. Evidently, the removal efficiencies achieved in the fixed-bed column experiments were lower than those observed in the batch method. This discrepancy was likely associated with the extended contact time of the pollutants in the batch process.[74] Additionally, no significant swelling of EC–AB was observed throughout the duration of the column experiments.

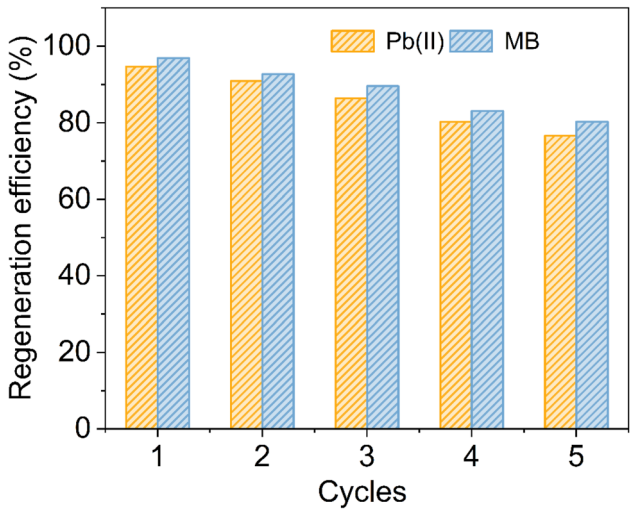

Fig. 10 Regeneration of EC–AB for Pb(II)/MB adsorption.

3.5 Regeneration studies

The results indicated that the adsorption capacities of Pb(II) and MB decreased as the number of regeneration cycles increased, as shown in Fig. 10. Following the first regeneration cycle, the removal efficiency was 94.63% for Pb(II) and 96.88% for MB. After the fifth cycle, the removal efficiencies were 76.64% for Pb(II) and 80.29% for MB, demonstrating the potential reusability of the EC–AB adsorbent. This decline in efficiency was attributed to the incomplete desorption of the heavy metals and dyes during regeneration. Additionally, the acidic or basic solution employed to facilitate desorption potentially caused some degradation of the chitosan structure, thereby decreasing the quantity of active binding sites available for adsorption.

3.6 Adsorption mechanism

To gain a deep understanding of the adsorption mechanism of the adsorbent, the EC–AB adsorbent was analyzed before and after Pb(II)/MB adsorption by SEM/EDS, FTIR spectra and XPS, respectively. SEM and EDS elemental mapping were performed for Pb-EC–AB and MB-EC–AB (see Fig. S2 and Table S2†). The

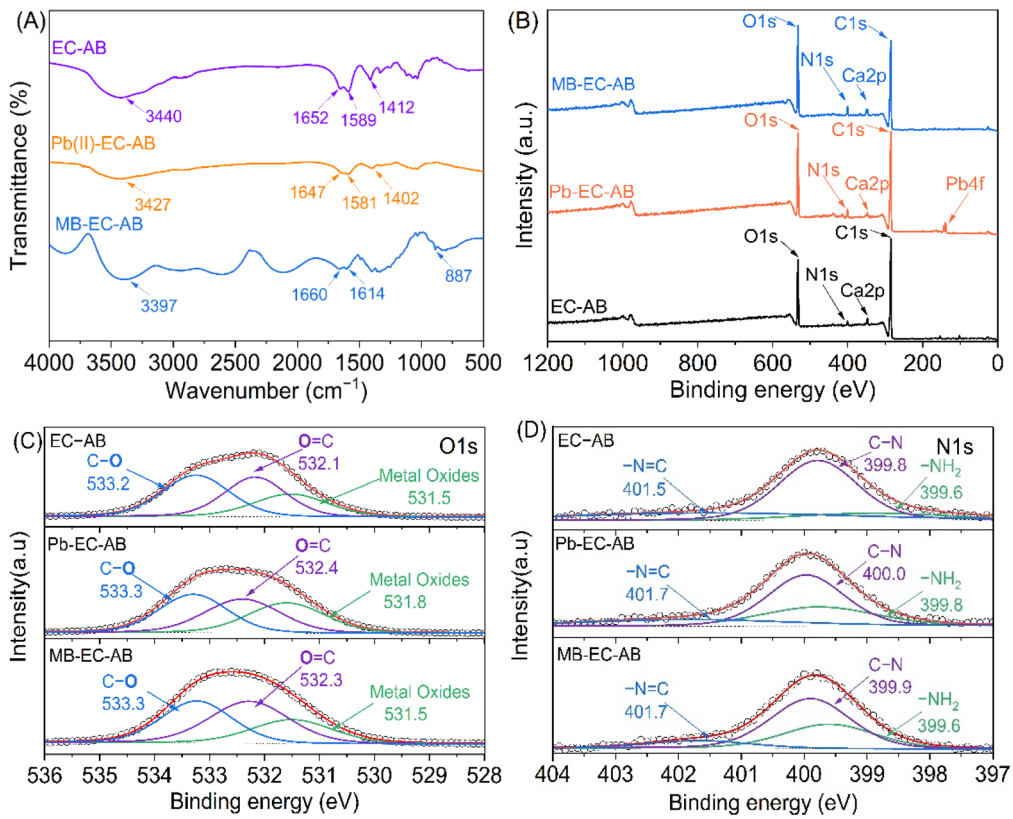

Fig. 11 Characterization of EC–AB before and after the adsorption of Pb(II)/MB: (A) FTIR spectra; (B) full-range XPS spectra; high-resolution XPS spectra of the O 1s (C) and N 1s (D) regions.

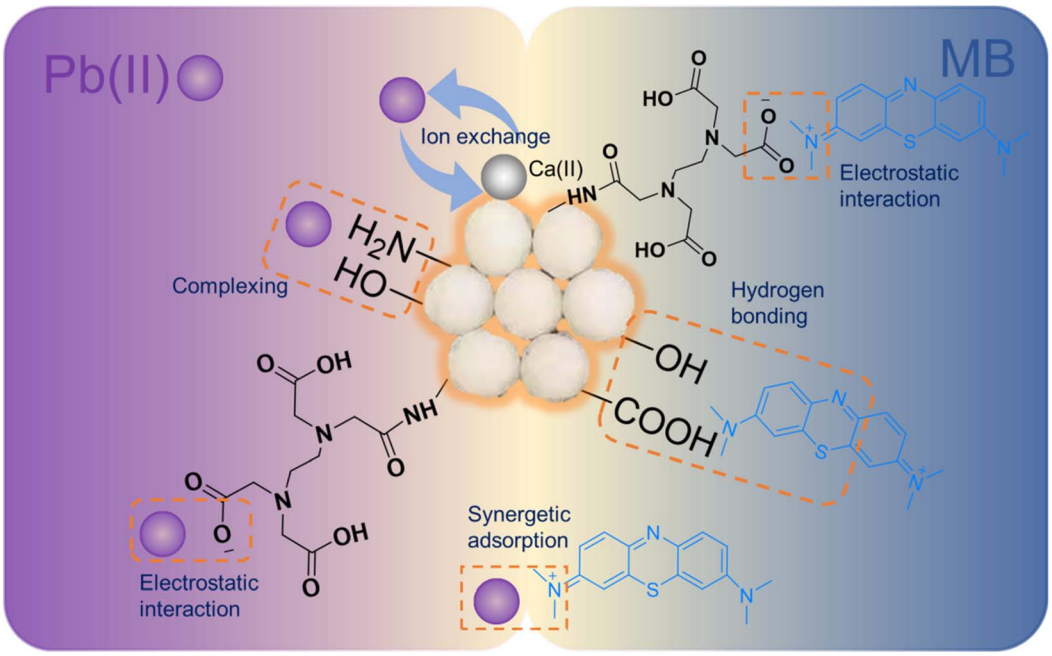

Fig. 12 Possible adsorption mechanism of Pb(II) and MB removal by EC–AB.

SEM images show that Pb-EC–AB and MB-EC–AB retained the morphological features of EC–AB, showing typical spherical particles with a fragmented surface with a porous structure (Fig. 2), indicating that EC–AB remained stable during the adsorption process. The EDS elemental mapping revealed a homogeneous distribution of Pb, S and Cl, suggesting that Pb(II)/MB was evenly adsorbed on the EC–AB surface. Notably, the mass proportion of Ca in Pb-EC–AB was significantly lower than that in EC–AB, which may be attributed to ion-exchange interactions between Ca(II) and Pb(II).

As shown in Fig. 11A, the overlapping peaks at 3440 cm^{-1}, which were attributed to the stretching vibration of the –OH and $–NH_2$ groups (EC–AB), shifted to 3427 cm^{-1} for Pb-EC–AB and 3397 cm^{-1} for MB-EC–AB, indicating that all of these groups may interact with Pb(II) and MB.[5] The peaks at 1652 cm^{-1}, 1589 cm^{-1}, and 1412 cm^{-1}, which are ascribed to the carboxyl groups and tertiary amine groups of EDTA fragments, as well as the amino groups of chitosan fragments, also weakened. This might be due to the fact that Pb(II) ions may interact with the carboxyl groups through electrostatic attraction and chelation.[58,60] For MB-EC–AB, a new characteristic peak was observed at 887 cm^{-1}, corresponding to the out-of-plane vibration of the =C–H strain of MB,[75] confirming that the dye molecules were adsorbed on the adsorbent.

Fig. 11B shows the XPS spectra of EC–AB before and after the adsorption. A distinct Pb4f peak at 138.4 eV appeared in the spectrum of EC–AB after adsorption, confirming the successful adsorption of Pb(II) onto EC–AB. The typical Ca 2p peak of the hydrogel with a bonding energy of 346.8 eV almost disappeared after the adsorption,[76] suggesting ion exchange between Ca(II) and Pb(II) during the process, consistent with the EDS results. The high-resolution O 1s spectrum of EC–AB was deconvoluted into three peaks (Fig. 11C): 533.2 eV (C–O), 532.1 eV (C=O), and 531.5 eV (Ca–O). After Pb(II) adsorption, these peaks shifted to 533.3, 532.4, and 531.6 eV,[72] respectively, with the proportion of metal oxides (Ca–O and Pb–O) increasing from 24% to 31%. Following MB adsorption, all the peaks except those of metal oxides exhibited similar shifts. The increased binding energy indicated that the oxygen atoms in the C–O and C=O groups of EC–AB participated in coordinating with Pb(II) and MB. In the high-resolution N 1s spectrum (Fig. 11D), EC–AB displayed three sub peaks at 401.5 eV (–N=C), 399.8 eV (N–C) and 399.6 eV ($–NH_2$), respectively.[77] After Pb(II) adsorption, the peaks of –N=C, N–C and $–NH_2$ were shifted to 401.7, 400.0 and 399.8 eV, respectively, which was due to the binding of Pb(II) ions to the nitrogen atoms in EC–AB, decreasing the electron density with respect to the nitrogen atoms and increasing the binding energy.[78–80] A comparable trend was observed after MB adsorption. Based on these results, a schematic diagram of the adsorption of MB and Pb(II) contaminants on EC–AB adsorbent was prepared to clarify the multi-binding-interactions between the adsorbent and contaminants, as shown in Fig. 12. This diagram show that for MB and Pb(II), electrostatic attraction, chelation, ion exchange, H-bonding and synergistic effects were all involved in the adsorption process.

4. Conclusions

A novel EDTA-chitosan/alginate porous composite bead adsorbent was synthesized for the simultaneous removal of Pb(II) and MB. Characterization results revealed that the EC–AB adsorbent possessed a porous structure with a high specific surface area (27.9 $m^2\ g^{-1}$) and abundant functional groups ($–NH_2$, –COOH, and –OH), as confirmed by BET analysis, FTIR, and XPS. Results showed that the prepared EC–AB adsorbent exhibited good adsorption performance for Pb(II) and MB. The adsorption

isotherm data fitted well with the Langmuir model, with maximum adsorption capacities of 504.11 mg g^{-1} for Pb(II) and 660.76 mg g^{-1} for MB. The adsorption process followed the pseudo-second-order kinetic model. The results of the adsorption isotherms, kinetics and mechanism investigations demonstrated that physical adsorption and chemical adsorption (electrostatic attraction, complexation, hydrogen bonding and ion exchange) were involved in the adsorption of Pb(II) and MB. Furthermore, the EC–AB adsorbent demonstrated excellent reusability for five cycles, with the adsorption capacities for Pb(II) and MB declining by only 23.56% and 19.71%, respectively. These results highlight the potential of the proposed adsorbent for application in real-world scenarios.

Data availability

All the data and research presented in this manuscript represent the work of a review paper with full citations to all original research presented and clearly indicated. All the data presented in this research are open access and available for access upon redirecting to the appropriate reference and resource.

Author contributions

Xueling Liu: formal analysis, investigation, and writing – original draft. Wenjie Ren: investigation and visualization. Weilin Song: investigation and validation. Wanqiang Zhang: data curation validation. Yuhan Wang: formal analysis and resources. Yi Wang: project administration and supervision. Guozhi Fan: project administration. Lei Zhang: conceptualization, funding acquisition, methodology, and writing – review & editing. Yanjun Huang: methodology, supervision, and writing – review & editing.

Conflicts of interest

The authors declare that they have no known competing financial interests or personal relationships that could have appeared to influence the work reported in this paper.

Acknowledgements

The authors express their sincere thanks to the Scientific Research Foundation of Wuhan Polytechnic University (grant no. 118-53210052144) and the ESI Discipline Construction Project of Wuhan Polytechnic University (grant no. 01003009). The authors would like to thank the Shiyanjia Lab (**https://www.shiyanjia.com**) for the characteristic analysis.

References

1 J. Deng, X. Zhang, G. Zeng, J. Gong, Q. Niu and J. Liang, Simultaneous removal of Cd(II) and ionic dyes from aqueous solution using magnetic graphene oxide nanocomposite as an adsorbent, *Chem. Eng. J.*, 2013, **226**, 189–200.

2 T. Shi, Z. Xie, Z. Zhu, W. Shi, Y. Liu, M. Liu and X. Mo, Effective removal of metal ions and cationic dyes from aqueous solution using different hydrazine–dopamine modified sodium alginate, *Int. J. Biol. Macromol.*, 2022, **195**, 317–328.

3 Z. Chen, X. Huo, G. Chen, X. Luo and X. Xu, Lead (Pb) exposure and heart failure risk, *Environ. Sci. & Pollut. Res.*, 2021, **28**, 28833–28847.

4 C. Zeng, H. Hu, X. Feng, K. Wang and Q. Zhang, Activating $CaCO_3$ to enhance lead removal from lead-zinc solution to serve as green technology for the purification of mine tailings, *Chemosphere*, 2020, **249**, 126227.

5 Y. Chen, Z. Nie, J. Gao, J. Wang and M. Cai, A novel adsorbent of bentonite modified chitosan-microcrystalline cellulose aerogel prepared by bidirectional regeneration strategy for Pb(II) removal, *J. Environ. Chem. Eng.*, 2021, **9**, 105755.

6 K. G. Pavithra, P. S. Kumar, V. Jaikumar and P. S. Rajan, Removal of colorants from wastewater: A review on sources and treatment strategies, *J. Chem. Ind. Eng.*, 2019, **75**, 1–19.

7 X. Li, Q. Zhang and B. Yang, Co-precipitation with $CaCO_3$ to remove heavy metals and significantly reduce the moisture content of filter residue, *Chemosphere*, 2020, **239**, 124660.

8 P. Goyal, C. S. Tiwary and S. K. Misra, Ion exchange based approach for rapid and selective Pb(II) removal using iron oxide decorated metal organic framework hybrid, *J. Environ. Manag.*, 2021, **277**, 111469.

9 A. A. Gouda, R. El Sheikh, A. O. Youssef, N. Gouda, W. Gamil and H. A. Khadrajy, Preconcentration and separation of Cd(II), Co(II), Cu(II), Ni(II), and Pb(II) in environmental samples on cellulose nitrate membrane filter prior to their flame atomic absorption spectroscopy determinations, *Int. J. Environ. Anal. Chem.*, 2020, **103**, 364–377.

10 J. Cheng, C. Zhan, J. Wu, Z. Cui, J. Si, Q. Wang, X. Peng and L.-S. Turng, Highly efficient removal of methylene blue dye from an aqueous solution using cellulose acetate nanofibrous membranes modified by polydopamine, *ACS Omega*, 2020, **5**, 5389–5400.

11 S. Sharan, P. Khare, R. Shankar, A. Tyagi and A. Khare, Development of 3D network of Zn-oxide nanorods assisted with PbO_2/Pb electrode for electrochemical oxidation of methylene blue in aqueous phase, *J. Taiwan Inst. Chem. Eng.*, 2023, **144**, 104739.

12 R. Choumane and S. Peulon, Development of an efficient electrochemical process for removing and separating soluble Pb(II) in aqueous solutions in presence of other heavy metals: Studies of key parameters, *Chem. Eng. J.*, 2021, **423**, 130161.

13 L. P. Mazur, M. A. P. Cechinel, S. M. A. G. U. de Souza, R. A. R. Boaventura and V. J. P. Vilar, Brown marine macroalgae as natural cation exchangers for toxic metal removal from industrial wastewaters: A review, *J. Environ. Manage.*, 2018, **223**, 215–253.

14 G. Reimonn and J. Kamcev, Techno-economic perspective on the limitations and prospects of ion-exchange membrane technologies, *Curr. Opin. Chem. Eng.*, 2025, **47**, 101077.

15 X. Zhou, X. Li, D. Yang, X. Jing, W. Yan and H. Xu, Bipolar Membranes: A review on principles, preparation methods

and applications in environmental and resource recovery, *Chem. Eng. J.*, 2025, **507**, 160184.

16 R. Choumane and S. Peulon, Innovative electrochemical process for a total removal and/or separation of soluble heavy metals, *J. Environ. Chem. Eng.*, 2022, **10**, 108607.

17 T. Pei, F. Shi, C. Liu, Y. Lu, X. Lin, D. Hou, S. Yang, J. Li, Z. Zheng and Y. Zheng, Bamboo-derived nitrogen-doping magnetic porous hydrochar coactivated by K_2FeO_4 and $CaCO_3$ for phenol removal: Governing factors and mechanisms, *Environ. Pollut.*, 2023, **331**, 121871.

18 C. Sun, T. Chen, Q. Huang, J. Wang, S. Lu and J. Yan, Enhanced adsorption for Pb(II) and Cd(II) of magnetic rice husk biochar by $KMnO_4$ modification, *Environ. Sci. Pollut.*, 2019, **26**, 8902–8913.

19 J. Wang and S. Zhuang, Chitosan-based materials: Preparation, modification and application, *J. Clean. Prod.*, 2022, **355**, 131825.

20 A. K. Mallik, S. M. F. Kabir, F. B. Rahman, M. N. Sakib, S. S. Efty and M. M. Rahman, Cu(II) removal from wastewater using chitosan-based adsorbents: A review, *J. Environ. Chem. Eng.*, 2022, **10**, 108048.

21 M. Ahmad, K. Manzoor and S. Ikram, Versatile nature of hetero-chitosan based derivatives as biodegradable adsorbent for heavy metal ions; A review, *Int. J. Biol. Macromol.*, 2017, **105**, 190–203.

22 S. Wang, Y. Liu, Y. Hu and W. Shen, A magnetic MIL-125-NH_2@chitosan composite as a separable adsorbent for the removal of Cr(VI) from wastewater, *Int. J. Biol. Macromol.*, 2023, **226**, 1054–1065.

23 I. P. S. Fernando, W. Lee, E. J. Han and G. Ahn, Alginate-based nanomaterials: Fabrication techniques, properties, and applications, *Chem. Eng. J.*, 2019, **391**, 123823.

24 G. Kayan and A. Kayan, Composite of natural polymers and their adsorbent properties on the dyes and heavy metal ions, *J. Polym. Environ.*, 2021, **29**, 3477–3496.

25 L. Jiang, D. Zhou, J. Yang, S. Zhou, H. Wang, X. Yuan, J. Liang, X. Li, Y. Chen and H. Li, 2D single- and few-layered MXenes: synthesis, applications and perspectives, *J. Mater. Chem. A*, 2022, **10**, 13651–13672.

26 Z. Shao, X. Huang, F. Yang, W. Zhao, X. Zhou and C. Zhao, Engineering sodium alginate-based cross-linked beads with high removal ability of toxic metal ions and cationic dyes, *Carbohydr. Polym.*, 2018, **187**, 85–93.

27 H. Masoumi, A. Ghaemi and H. G. Gilani, Evaluation of hyper-cross-linked polymers performances in the removal of hazardous heavy metal ions: A review, *Sep. Purif. Technol.*, 2021, **260**, 118221.

28 L. Tan, Y. Nie, H. Chang, L. Zhu, K. Guo, X. Ran, N. Zhong, D. Zhong, Y. Xu and S.-H. Ho, Adsorption performance of Ni(II) by KOH-modified biochar derived from different microalgae species, *Bioresour. Technol.*, 2024, **394**, 130287.

29 X. Liu, Y. Wang, X. Wu, Y. Wang, G. Fan, Y. Huang and L. Zhang, Preparation of magnetic DTPA-modified chitosan composite microspheres for enhanced adsorption of Pb(II) from aqueous solution, *Int. J. Biol. Macromol.*, 2024, **264**, 130410.

30 X. Li, S. Wang, Y. Liu, L. Jiang, B. Song, M. Li, G. Zeng, X. Tan, X. Cai and Y. Ding, Adsorption of Cu(II), Pb(II), and Cd(II) ions from acidic aqueous solutions by diethylenetriaminepentaacetic acid-modified magnetic graphene oxide, *J. Chem. Eng. Data*, 2016, **62**, 407–416.

31 E. Repo, R. Koivula, R. Harjula and M. Sillanpää, Effect of EDTA and some other interfering species on the adsorption of Co(II) by EDTA-modified chitosan, *Desalination*, 2013, **321**, 93–102.

32 P. Sun, W. Zhang, B. Zou, L. Zhou, Z. Ye and Q. Zhao, Preparation of EDTA-modified magnetic attapulgite chitosan gel bead adsorbent for the removal of Cu(II), Pb(II), and Ni(II), *Int. J. Biol. Macromol.*, 2021, **182**, 1138–1149.

33 S. Li, Y. Li, Z. Fu, L. Lu, J. Cheng and Y. Fei, A 'top modification' strategy for enhancing the ability of a chitosan aerogel to efficiently capture heavy metal ions, *J. Colloid Interface Sci.*, 2021, **594**, 141–149.

34 W. Zhang, J. Ou, M. Tang, Q. He, A. Long, S. Luo, S. Sun, J. Wan, Y. Gao, L. Zhou, B. Wang and H. Wang, Physically-crosslinked activated $CaCO_3$/polyaniline-polypyrrole-modified GO/alginate hydrogel sorbent with highly efficient removal of copper(II) from aqueous solution, *Chem. Eng. J.*, 2022, **431**, 133375.

35 B. Chen, H. Zhao, S. Chen, F. Long, B. Huang, B. Yang and X. Pan, A magnetically recyclable chitosan composite adsorbent functionalized with EDTA for simultaneous capture of anionic dye and heavy metals in complex wastewater, *Chem. Eng. J.*, 2019, **356**, 69–80.

36 X. Fan, X. Wang, Y. Cai, H. Xie, S. Han and C. Hao, Functionalized cotton charcoal/chitosan biomass-based hydrogel for capturing Pb^{2+}, Cu^{2+} and MB, *J. Hazard. Mater.*, 2022, **423**, 127191.

37 Y. Huang, H. Zheng, X. Hu, Y. Wu, X. Tang, Q. He and S. Peng, Enhanced selective adsorption of lead(II) from complex wastewater by DTPA functionalized chitosan-coated magnetic silica nanoparticles based on anion-synergism, *J. Hazard. Mater.*, 2022, **422**, 126856.

38 Y. J. Huang, H. L. Wu, T. K. Shao, X. Zhao, H. Peng, Y. F. Gong and H. H. Wan, Enhanced copper adsorption by DTPA-chitosan/alginate composite beads: Mechanism and application in simulated electroplating wastewater, *Chem. Eng. J.*, 2018, **339**, 322–333.

39 N. Souza, H. M. Brandao and L. F. C. de Oliveira, Spectroscopic and thermogravimetric study of chitosan after incubation in bovine rumen, *J. Mol. Struct.*, 2011, **1005**, 186–191.

40 Y. Ren, H. A. Abbood, F. He, H. Peng and K. Huang, Magnetic EDTA-modified chitosan/SiO_2/Fe_3O_4 adsorbent: Preparation, characterization, and application in heavy metal adsorption, *Chem. Eng. J.*, 2013, **226**, 300–311.

41 N. S. Surgutskaia, A. D. Martino, J. Zednik, K. Ozaltin, L. Lovecká, E. D. Bergerová, D. Kimmer, J. Svoboda and V. Sedlarik, Efficient Cu^{2+}, Pb^{2+} and Ni^{2+} ion removal from wastewater using electrospun DTPA-modified chitosan/polyethylene oxide nanofibers, *Sep. Purif. Technol.*, 2020, **247**, 116914.

42 B. Tanhaei, A. Ayati, F. F. Bamoharram and M. Sillanpää, Magnetic EDTA Functionalized Preyssler Cross Linked Chitosan Nanocomposite for Adsorptive Removal of Pb(II) Ions, *Clean: Soil, Air, Water*, 2017, **45**, 1700328.

43 L. W. Zheng, Y. C. Gao, J. H. Du, W. Zhang, Y. J. Huang, L. L. Wang, Q. Q. Zhao and X. L. Pan, A novel, recyclable magnetic biochar modified by chitosan-EDTA for the effective removal of Pb(ii) from aqueous solution, *RSC Adv.*, 2020, **10**, 40196–40205.

44 P. Sun, W. Zhang, B. Z. Zou, L. C. Zhou, Z. F. Ye and Q. L. Zhao, Preparation of EDTA-modified magnetic attapulgite chitosan gel bead adsorbent for the removal of Cu(II), Pb(II), and Ni(II), *Int. J. Biol. Macromol.*, 2021, **182**, 1138–1149.

45 E. Tao, D. Ma, S. Yang and X. Hao, Graphene oxide-montmorillonite/sodium alginate aerogel beads for selective adsorption of methylene blue in wastewater, *J. Alloys Compd.*, 2020, **832**, 154833.

46 W. S. W. Ngah and S. Fatinathan, Adsorption of Cu(II) ions in aqueous solution using chitosan beads, chitosan-GLA beads and chitosan-alginate beads, *Chem. Eng. J.*, 2008, **143**, 62–72.

47 W. Yang, Y. Liu, Y. Zhu, W. Jiang, F. Shi, J. Hu, S. Jiang and S. Jian, Epichlorohydrin and triethylenetetramine functionalized electrosprayed Fe3O4/Chitosan magnetic microspheres for removal and separation of Congo red, *Chem. Eng. J.*, 2023, **476**, 146907.

48 D. Wu, L. Hu, Y. Wang, Q. Wei, L. Yan, T. Yan, Y. Li and B. Du, EDTA modified β-cyclodextrin/chitosan for rapid removal of Pb(II) and acid red from aqueous solution, *J. Colloid Interface Sci.*, 2018, **523**, 56–64.

49 L. Zhang, Q. Li, J. Zhu, H. Liu, X. Liu, Y. Wang, G. Fan, Y. Huang and L. Li, H_2O_2 modified peanut shell-derived biochar/alginate composite beads as a green adsorbent for removal of Cu(II) from aqueous solution, *Int. J. Biol. Macromol.*, 2023, **240**, 124466.

50 D. Li, T. Hua, J. Yuan and F. Xu, Methylene blue adsorption from an aqueous solution by a magnetic graphene oxide/humic acid composite, *Colloids Surf., A*, 2021, **627**, 127171.

51 J. Ma, G. Zhou, L. Chu, Y. Liu, C. Liu, S. Luo and Y. Wei, Efficient removal of heavy metal ions with an EDTA functionalized chitosan/polyacrylamide double network hydrogel, *ACS Sustainable Chem. Eng.*, 2016, **5**, 843–851.

52 A. Rahmatpour and N. Alijani, An all-biopolymer self-assembling hydrogel film consisting of chitosan and carboxymethyl guar gum: A novel bio-based composite adsorbent for Cu^{2+} adsorption from aqueous solution, *Int. J. Biol. Macromol.*, 2023, **242**, 124878.

53 X. Xu, X. Ouyang and L. Yang, Adsorption of Pb(II) from aqueous solutions using crosslinked carboxylated chitosan/carboxylated nanocellulose hydrogel beads, *J. Mol. Liq.*, 2021, **322**, 114523.

54 Y. Du, Q. Lu, H. Chen, Y. Du and D. Du, A novel strategy for arsenic removal from dirty acid wastewater via $CaCO_3$-$Ca(OH)_2$-Fe(III) processing, *J. Water Process Eng.*, 2016, **12**, 41–46.

55 S. Lagergren, About the Theory of So-Called Adsorption of Soluble Substances, *Kungliga Svenska Vetenskapsakademiens Handlingar*, 1898, vol. 24, pp. 1–39.

56 Y. S. Ho and G. McKay, Sorption of aye from aqueous solution by peat, *Chem. Eng. J.*, 1998, **70**, 115–124.

57 W. J. Weber Jr and J. C. Morris, Kinetics of adsorption on carbon from solution, *Altern. Med. Rev.*, 1963, **2**, 31–59.

58 M. Verma, R. Borah, A. Kumar, S. H. Chae, S. Y. Pan, V. Kumar, M. S. Vlaskin and H. Kim, Capturing of inorganic and organic pollutants simultaneously from complex wastewater using recyclable magnetically chitosan functionalized with EDTA adsorbent, *Process Saf. Environ.*, 2022, **167**, 56–66.

59 N. H. Abdullah and A. Borhan, Efficient simultaneous biosorption of Pb(II), Cu(II), Cd(II), and oily solutions onto chitosan-coated rubber seed shell activated carbon: Optimization, isotherm, kinetic, and thermodynamic studies, *J. Water Process Eng.*, 2024, **68**, 106480.

60 S. T. Zhuang, Q. Zhang and J. L. Wang, Adsorption of Co^{2+} and Sr^{2+} from aqueous solution by chitosan grafted with EDTA, *J. Mol. Liq.*, 2021, **325**, 115197.

61 K. Xu, T. He, L. Li, J. Iqbal, Y. Tong, L. Hua, Z. Tian, L. Zhao and H. Li, DOTA functionalized adsorbent DOTA@Sludge@Chitosan derived from recycled shrimp shells and sludge and its application for lead and chromium removal from water, *Int. J. Biol. Macromol.*, 2024, **255**, 128263.

62 M. Verma, I. Lee, Y. Hong, V. Kumar and H. Kim, Multifunctional β-cyclodextrin-EDTA-chitosan polymer adsorbent synthesis for simultaneous removal of heavy metals and organic dyes from wastewater, *Environ. Pollut.*, 2022, **292**, 118447.

63 M. Usman, A. Ahmed, B. Yu, S. Wang, Y. Shen and H. Cong, Simultaneous adsorption of heavy metals and organic dyes by β-Cyclodextrin-Chitosan based cross-linked adsorbent, *Carbohydr. Polym.*, 2021, **255**, 117486.

64 I. H. Alsohaimi, M. S. Alhumaimess, A. A. Alqadami, H. M. A. Hassan, Q. Chen, M. S. Alamri, M. M. J. Alanzi and T. S. Alraddadi, Chitosan-carboxylic acid grafted multifunctional magnetic nanocomposite as a novel adsorbent for effective removal of methylene blue dye from aqueous environment, *Chem. Eng. Sci.*, 2023, **280**, 119017.

65 D. Guo, Q. An, Z. Xiao, S. Zhai and D. Yang, Efficient removal of Pb(II), Cr(VI) and organic dyes by polydopamine modified chitosan aerogels, *Carbohydr. Polym.*, 2018, **202**, 306–314.

66 L. D. B. Araújo, H. K. de Matos, D. P. Facchi, D. A. de Almeida, B. M. G. Gonçalves, J. P. Monteiro, A. F. Martins and E. G. Bonafé, Natural carbohydrate-based thermosensitive chitosan/pectin adsorbent for removal of Pb(II) from aqueous solutions, *Int. J. Biol. Macromol.*, 2021, **193**, 1813–1822.

67 D. Hu, Z. Lian, H. Xian, R. Jiang, N. Wang, Y. Weng, X. Peng, S. Wang and X. K. Ouyang, Adsorption of Pb(II) from aqueous solution by polyacrylic acid grafted magnetic chitosan nanocomposite, *Int. J. Biol. Macromol.*, 2020, **154**, 1537–1547.

68 B. Chen, F. Long, S. Chen, Y. Cao and X. Pan, Magnetic chitosan biopolymer as a versatile adsorbent for simultaneous and synergistic removal of different sorts of dyestuffs from simulated wastewater, *Chem. Eng. J.*, 2020, **385**, 123926.

69 N. Jian, Y. Dai, L. Liu, D. Wu, F. Qi and Y. Wu, Simultaneous extraction of multi-antibiotic residues in environmental water by DTPA-modified polyaniline nanofibers membrane, *Sep. Purif. Technol.*, 2022, **284**, 120271.

70 S. S. Elanchezhiyan, P. Karthikeyan, K. Rathinam, M. H. Farzana and C. M. Park, Magnetic kaolinite immobilized chitosan beads for the removal of Pb(II) and Cd(II) ions from an aqueous environment, *Carbohydr. Polym.*, 2021, **261**, 117892.

71 P. Wang, G. An, P. Jarvis, W. Liu, S. Ding, R. Qu, Z. Li, C. Ye and W. Chu, Simultaneous removal of organic micropollutants and metals from water by a multifunctional β-cyclodextrin polymer-supported-polyaniline composite, *Chem. Eng. J.*, 2024, **482**, 148826.

72 F. Zhao, E. Repo, D. Yin, Y. Meng, S. Jafari and M. Sillanpää, EDTA-cross-linked β-cyclodextrin: An environmentally friendly bifunctional adsorbent for simultaneous adsorption of metals and cationic dyes, *Environ. Sci. Technol.*, 2015, **49**, 10570–10580.

73 D. Yu, L. Wang and M. Wu, Simultaneous removal of dye and heavy metal by banana peels derived hierarchically porous carbons, *J. Taiwan Inst. Chem. Eng.*, 2018, **93**, 543–553.

74 Y. Hannachi and A. Hafidh, Preparation and characterization of novel bi-functionalized xerogel for removal of methylene blue and lead ions from aqueous solution in batch and fixed-bed modes: RSM optimization, kinetic and equilibrium studies, *J. Saudi Chem. Soc.*, 2020, **24**, 505–519.

75 M. S. Islam, M. S. Rahaman and B. Barbeau, Removal of Pb(II), Zn(II), Cu(II), and As (III) ions from water using kraft pulp-based carboxymethylated cellulose in a fixed-bed column adsorption process, *J. Environ. Chem. Eng.*, 2023, **11**, 111181.

76 K. Carrera, V. Huerta, V. Orozco, J. Matutes, P. Fernández, O. A. Graeve and M. Herrera, Formation of vacancy point-defects in hydroxyapatite nanobelts by selective incorporation of Fe^{3+} ions in Ca(II) sites. A CL and XPS study, *Mater. Sci. Eng., B*, 2021, **271**, 115308.

77 C. Bulin, T. Guo and R. Zheng, Preparation of ion imprinted EDTA modified chitosan-magnetic graphene oxide for selective recovery and adsorption mechanism of Ce(III), *Sci. Total Environ.*, 2025, **962**, 178468.

78 X. Zhao, H. Zhao, A. Mei, L. Peng and J. Sun, Novel chitosan/lignin hydrogel prepared by the Mannich reaction for Pb(II) and Cu(II) removal from aqueous solution, *Int. J. Biol. Macromol.*, 2025, **285**, 138177.

79 A. Benettayeb, S. Ghosh, M. Usman, F. Z. Seihoub, I. Sohoo, C. H. Chia and M. Sillanpää, Some Well-Known Alginate and Chitosan Modifications Used in Adsorption: A Review, *Water*, 2022, **14**, 26.

80 Y. Liu, R. Q. Fu, Y. Sun, X. X. Zhou, S. A. Baig and X. H. Xu, Multifunctional nanocomposites Fe_3O_4@SiO_2-EDTA for Pb(II) and Cu(II) removal from aqueous solutions, *Appl. Surf. Sci.*, 2016, **369**, 267–276.